Lava delta deformation as a proxy for submarine slope instability

Federico Di Traglia [a,*], Teresa Nolesini [a], Lorenzo Solari [a], Andrea Ciampalini [b],
William Frodella [a], Damiano Steri [a], Benedetto Allotta [c,d], Andrea Rindi [c,d],
Lorenzo Marini [d], Niccolò Monni [d], Emanuele Galardi [d], Nicola Casagli [a]

[a] *Dipartimento di Scienze della Terra, Università degli Studi di Firenze, Via La Pira 4, 50121, Firenze, Italy*
[b] *Dipartimento di Scienze della Terra, Università di Pisa, Via Santa Maria 53, 56126, Pisa, Italy*
[c] *Dipartimento di Ingegneria Industriale, Università degli Studi di Firenze, Via Santa Marta 3, 50139, Firenze, Italy*
[d] *MDM Team S.r.l., official Spin-off company of the Università degli Studi di Firenze, Via Venezia 4, 50121, Firenze, Italy*

A B S T R A C T

The instability of lava deltas is a recurrent phenomenon affecting volcanic islands, which can potentially cause secondary events such as littoral explosions (due to interactions between hot lava and seawater) and tsunamis. It has been shown that Interferometric Synthetic Aperture Radar (InSAR) is a powerful technique to forecast the collapse of newly emplaced lava deltas. This work goes further, demonstrating that the monitoring of lava deltas is a successful strategy by which to observe the long-term deformation of subaerial–submarine landslide systems on unstable volcanic flanks. In this paper, displacement measurements derived from Synthetic Aperture Radar (SAR) imagery were used to detect lava delta instability at Stromboli volcano (Italy). Recent flank eruptions (2002–2003, 2007 and 2014) affected the Sciara del Fuoco (SdF) depression, created a "stacked" lava delta, which overlies a pre-existing scar produced by a submarine–subaerial tsunamigenic landslide that occurred on 30 December 2002. Space-borne X-band COSMO-SkyMED (CSK) and C-band SENTINEL-1A (SNT) SAR data collected between February 2010 and October 2016 were processed using the SqueeSAR algorithm. The obtained ground displacement maps revealed the differential ground motion of the lava delta in both CSK and SNT datasets, identifying a stable area (characterized by less than 2 mm/y in both datasets) within the northern sector of the SdF and an unstable area (characterized by velocity fields on the order of 30 mm/y and 160 mm/y in the CSK and SNT datasets, respectively) in the central sector of the SdF. The slope stability of the offshore part of the SdF, as reconstructed based on a recently performed multibeam bathymetric survey, was evaluated using a 3D Limit Equilibrium Method (LEM). In all the simulations, Factor of Safety (F) values between 0.9 and 1.1 always characterized the submarine slope between the coastline and −250 m a.s.l. The critical surfaces for all the search volumes corresponded to the 30 December 2002 landslide, which involved the lava delta and its surrounding areas. InSAR data provided the post-effusive deformation field after the 2007 and 2014 flank eruptions, whereas LEM results highlighted that the accumulation of lava flows on the prone-to-failure SdF submarine slope is the main cause of the detected lava delta deformation. Lava delta instability, measured also at Pico Island (Azores) and Kilauea volcano (Hawaii), is evidence of the broader spectrum of instability phenomena that take place in the coastal or submarine area of the flanks of the volcanoes. At Kilauea, past lava deltas have moved faster than the surrounding slope and the recorded movements relate only to the collapses of the deltas themselves, producing rapid mass wasting near the coasts. In contrast, at Stromboli and Pico, lava deltas move at the same velocity as the surrounding slope. In these cases, the displacement at lava deltas can be considered as a proxy for the deformation of submarine slides. There are very few studies dealing with lava delta deformation, thus, the analysis presented in this work will benefit the monitoring of submarine slopes in other prone-to-failure coastal or island volcanic systems which have the potential to generate tsunamis.
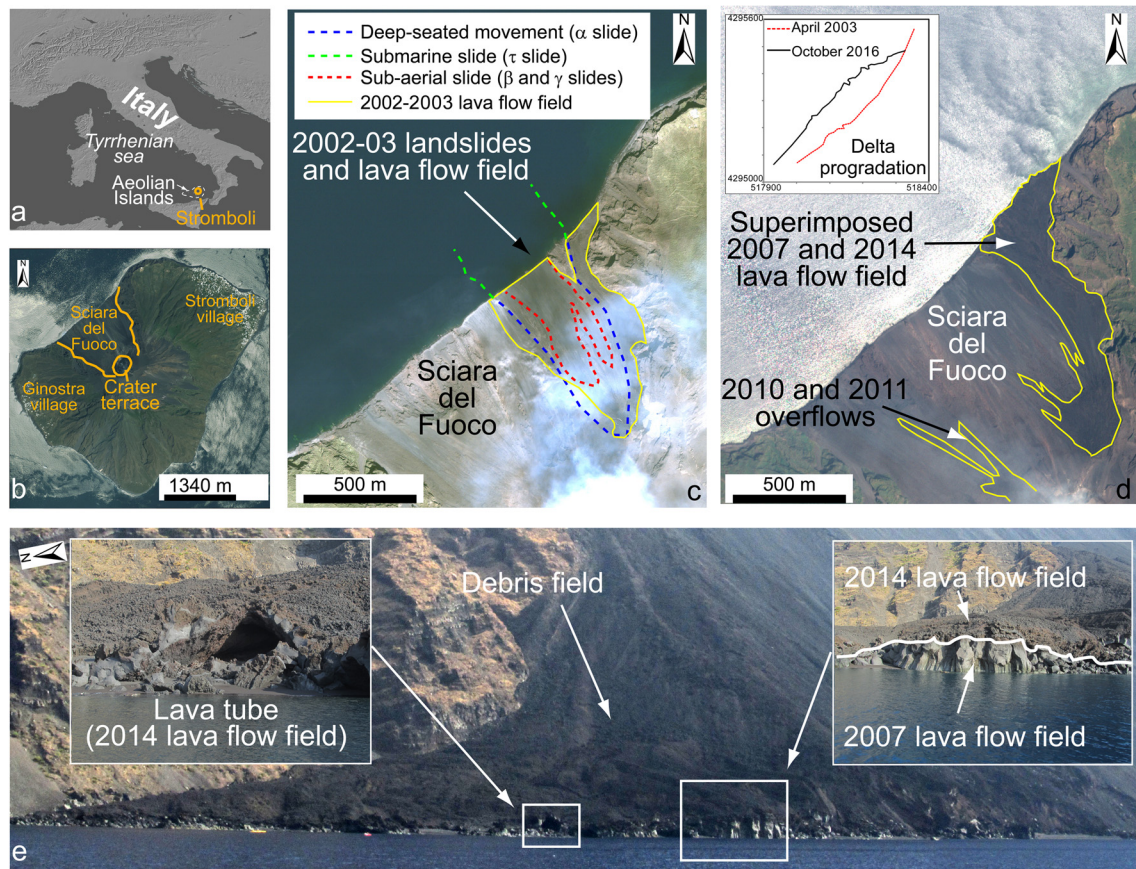
1. Introduction

Lava deltas, formed by the accumulation of lava flows within the sea or a lake (Richards, 1959; Nemec, 1990; Lipman and

* Corresponding author.
  E-mail address: federico.ditraglia@unifi.it (F. Di Traglia).

Fig. 1. a) Location of the Island of Stromboli within the central Mediterranean area; b) the Island of Stromboli. The main active geological features (Sciara del Fuoco and the crater terrace) and the two village areas are highlighted; c) IKONOS image collected on April 2003, emphasizing the 30 December 2002 landslide scarps, which are partially buried by the 2002–2003 lava flow field; d) PLEIADESNT image collected on May 2016, highlighting the superimposed 2007 and 2014 lava flow fields; the progradation of the lava delta, derived from the comparison between c) and d), is also shown; e) the present-day "stacked" lava delta (photo collected on October 2016 during the bathymetric survey), comprising the 2007 "low-elevation vent" lava flow (with a massive "aa lava flow" at the base) and the "high-elevation vent" lava flow, which consists of thin basal pahoehoe lava flows and extensive debris deposits produced by lava crumbling on the SdF extremely steep slope.

Moore, 1996; Ramalho et al., 2013; Bosman et al., 2014), are frequently unstable and delta collapses can potentially cause secondary hazardous events, such as littoral explosions and tsunamis (Jurado-Chichay et al., 1996; Mattox and Mangan, 1997; Chiocci et al., 2008a; Hildenbrand et al., 2012; Poland and Orr, 2014). Lava delta instability has been measured at Kilauea volcano (Hawaii), occurring since the emplacement and ending after complete collapse of the delta (Poland and Orr, 2014), and at Pico Island (Azores), associated with the creep of the southeastern flank of the island (Hildenbrand et al., 2012). Steep delta slopes are subject to frequent instability (failure) events, ranging from slow slope creep (i.e., slow, intergranular frictional sliding due to low strain rate) to fast moving debris flows (i.e., high strain rate), eventually evolving into turbidites (Nemec, 1990). This paper provides evidence that the study of long-term lava deltas deformation by means of the Interferometric Synthetic Aperture Radar (InSAR) data is fundamental to the monitoring of the stability of the submarine slopes in prone-to-failure coastal or island volcanic systems. Stromboli volcano was chosen as test-site, representing an optimal environmental setting and a case history of volcano slope instability phenomena where this methodology can be tested. The combination of displacement monitoring and slope stability modelling revealed that the observed deformation is related to the instability of the submarine slope. The proposed combination of field-based observations and advanced techniques, such as remote sensing and numerical modelling, provides information about both cause and extent of the detected lava delta deformation field, and it can be considered as a proxy for the deformation of submarine slides.

2. Case study: Stromboli

Stromboli is a volcanic island located in the Tyrrhenian Sea, off the southern coast of Italy (Fig. 1a). The entire volcanic edifice is $\approx$3 km high above the sea bottom and it is located at the NE tip of the Aeolian archipelago. It belongs to a late Quaternary, large volcanic complex of mostly basaltic to basaltic–andesitic composition (Tibaldi et al., 2009). The volcanic edifice has been affected by several episodes of sector collapse, the most relevant of which occurred ca. 13 ka in the NW part of the volcanic edifice, and which created the SdF depression (Tibaldi et al., 2009). Another large collapse event occurred at 5.6 ± 3.3 ka (Tibaldi et al., 2009), producing a massive landslide (0.73 ± 0.22 km^3, Di Roberto et al., 2010). The SdF depression is a landslide scar that extends down to 700 m below the sea level on the NW flank of the volcano and it is partially filled with volcaniclastic deposits and lavas (Kokelaar and Romagnoli, 1995; Rotonda et al., 2009; Nolesini et al., 2013) emitted from a summit crater terrace located at $\approx$750 m a.s.l. and from ephemeral vents located within the SdF (Fig. 1b; Marsella et al., 2012). Here, eruptive activity consists of typical persistent Strombolian activity, which is characterized by intermittent explosions from three vent zones (NE, SW and Central craters) located in the summit crater terrace (Calvari et al., 2014). This persistent Strombolian activity is often punctuated by periods dominated by stronger explosions and lava overflows from the crater terrace, and/or by lava flows from ephemeral vents (flank eruptions), as recently occurred in 2002–2003, 2007 and 2014 (Calvari et al., 2005; Marsella et al., 2012; Zakšek et al., 2015). During the 2002–2003

flank eruption, a submarine–subaerial landslide sequence (Fig. 1c; total volume of $25–30 \times 10^6$ m^3, Bonaccorso et al., 2003; Chiocci et al., 2008a) generated two tsunamis, which affected the coastline with a maximum run-up of 6–7 m at the Stromboli village (Tinti et al., 2006). These tsunamis were caused by an initial submarine rotational slide (τ slide, composed of two coalescing slides, τ_1 and τ_2 in Chiocci et al., 2008a) that affected the underwater volcaniclastic apron down to a depth of 350 m (Chiocci et al., 2008a), as well as by a second subaerial translational slide ($\beta + \gamma$ slides in Tommasi et al., 2005; Fig. 1c). Both the submarine and subaerial slides were caused by large deep-seated gravitational slope deformations (α slide in Tommasi et al., 2005; Fig. 1c) triggered by the injection of a lateral intrusion (Bonaccorso et al., 2003). The α slide developed under drained conditions, preventing the collapse of the entire α block (Chiocci et al., 2008a); during its continuous displacement, excessive pore pressure was likely generated in the τ slide (undrained load condition), reducing the effective stresses down to values compatible with the static liquefaction of the material (Tommasi et al., 2005; Boldini et al., 2009). Finally, subaerial $\beta + \gamma$ slides were induced by the foot removal by the τ slide (Chiocci et al., 2008a).

After the 2002–2003 eruption, another flank eruption began on 27 February 2007 with the opening of a first ephemeral vent at 650 m a.s.l. at the base of the NE crater area, which was followed by the opening of a second ephemeral vent at 400 m a.s.l. within the SdF (Marsella et al., 2012). The most recent flank eruption started on 7 August 2014 and lasted until 13 November 2014 (Di Traglia et al., 2018), with the emplacement of 7.4×10^6 m^3 of lava on the SdF from a fracture located at 650 m a.s.l. (Fig. 1d; Zakšek et al., 2015).

Recent flank eruptions at Stromboli have been characterized by ephemeral vents located in the SdF at elevations ranging from $\approx$350 m (1967 eruption; Marsella et al., 2012) to $\approx$670 m a.s.l. (1985 eruption; Marsella et al., 2012). During effusions characterized by high-elevation vents (600–670 m a.s.l.), lava flows reached the sea during the initial phase (high-effusion rate phase; Zakšek et al., 2015), producing small lava deltas (less than 50 m from the coastline; Marsella et al., 2012). Eruptions characterized by low-elevation vents (down to 350 m a.s.l.), such as the 1967 and 2007 flank eruptions, built up greater deltas (up to 100 m from the coastline; Marsella et al., 2012), while the entrance of lava flows into the sea and their interactions with seawater led to littoral explosions. The latter directly produced large quantities of volcaniclastic deposits caused by the quenching and the fragmentation processes that occurred in the offshore portion of the SdF (Bosman et al., 2014). During the 2007 eruption, the volume of erupted material ($\approx$10 $\times$ 10^6 m^3) mainly gathered underwater ($\approx$70%), rather than subaerially ($\approx$30%; Marsella et al., 2012; Bosman et al., 2014). Recent flank eruptions (2002–2003, 2007 and 2014) produced a "stacked" lava delta on a scar generated by submarine–subaerial tsunamigenic landslides that occurred on 30 December 2002 (Fig. 1c, d, e). However, lava deltas at Stromboli are commonly short-lasting features, as they are commonly eroded away by the sea within a few months/years, as it was demonstrated by the lack of recognizable lava deltas at the shoreline and in shallow water areas before the 2002–2003 eruption (Kokelaar and Romagnoli, 1995; Casalbore et al., 2010; Marsella et al., 2012; Bosman et al., 2014).

3. Material and methods

InSAR data, collected between February 2010 and October 2016 and processed using the SqueeSAR algorithm (Ferretti et al., 2011; Fig. 2), provided the post-effusive deformation field following the 2007 and 2014 flank eruptions. Based on a recently performed multibeam bathymetric survey, the stability of the submerged

lava delta sector was investigated using the 3D Limit Equilibrium Method (LEM).

3.1. Space-borne InSAR

Space-borne Interferometric SAR (InSAR) is an advanced geodetic technique that is mainly used to construct Digital Elevation Models (DEM) (i.e., Stevens et al., 2001) and/or to measure the ground motions that occurred in a certain time interval (Massonnet and Feigl, 1998). When mapping ground movement, InSAR technology is usually referred to as Differential InSAR (D-InSAR), although this only yields the displacement projected along the Line Of Sight (LOS) direction (Crosetto et al., 2016). The interferometric phase can be corrupted by noise (decorrelation) caused by contributions from the sum of different scatterers between SAR acquisitions. Signal decorrelation can be related to different factors (e.g., temporal and geometric decorrelation, volume scattering, atmospheric artefacts and processing error), and it is estimated by calculating the "coherence" (with values ranging from 0–1) between two acquisitions (Zebker et al., 1996). Displacements can be better estimated by processing a long stack of images using MT-InSAR algorithms such as Permanent Scatterer Interferometry (PSInSAR) (Ferretti et al., 1999, 2001), rather than by using two-image approaches (Crosetto et al., 2016). In this work, the SqueeSAR algorithm, which represents the technological evolution of the PSInSAR technique (Ferretti et al., 2011; Fig. 2), was used. The SqueeSAR algorithm analyses targets from a radar imaging dataset and it involves not only the identification of coherent Permanent Scatterers (PS; i.e., small parts of the study area that exhibit coherent phase behaviour) but also that of partially coherent Distributed Scatterers (DS). PS usually correspond to man-made objects (e.g., buildings, linear structures, and open outcrops), whereas DS, which are all pixels belonging to a certain surface with similar and common radar returns and displacement vectors (Ferretti et al., 2011), typically correspond to homogeneous ground surfaces, uncultivated regions, desert or debris-covered areas and scattered outcrops (Ferretti et al., 2011). A space adaptive filtering procedure (DespecKS), based on a statistical test able to discriminate whether two pixels are *statistically homogeneous* (Ferretti et al., 2011), is applied to the stack of SAR images. The Kolmogorov–Smirnov (KS) test (Kwam and Vidakovic, 2007) is the solution used to select these statistically homogeneous pixels (SHP) within a certain search window (usually one hectare large). This test is performed directly on the amplitude values of each pixel and it is used to connect all the pixels that record common radar characteristics with the pixel considered (which is the centre of the search window). All the SHP are then considered as a homogeneous population and further analysed. After selecting the SHP, the DespecKS algorithm allows us to i) average the amplitude or intensity values of each set of DS and reduce the speckle noise of the homogeneous areas without modifying the pointwise targets (i.e., the pixels referred to PS); and to ii) estimate the complex coherence matrix of every set of SHP (Ferretti et al., 2011). The phase triangulation algorithm (PTA, Ferretti et al., 2011) is applied to the coherence matrices of every DS to optimize the phase values of the original stack of SAR images and to perform the 3D phase unwrapping (Hooper and Zebker, 2007). Finally, the PS and DS are jointly processed using the PSInSAR procedure (Ferretti et al., 2001). In this work, a total of 84 SAR images from the X-band (9.6 GHz), COSMO-SkyMED (CSK) constellation (22 February 2010–18 December 2014) and 47 SAR images from the C-band (5.6 GHz) SENTINEL-1A (SNT) satellite (23 February 2015–October 15 2016) were used (Fig. 2). Fig. 2 also shows the localization of the reference point, which was chosen out of the SdF depression, in an area where no slope movements have been historically registered or are expected. Applying InSAR techniques can be a challenging task in
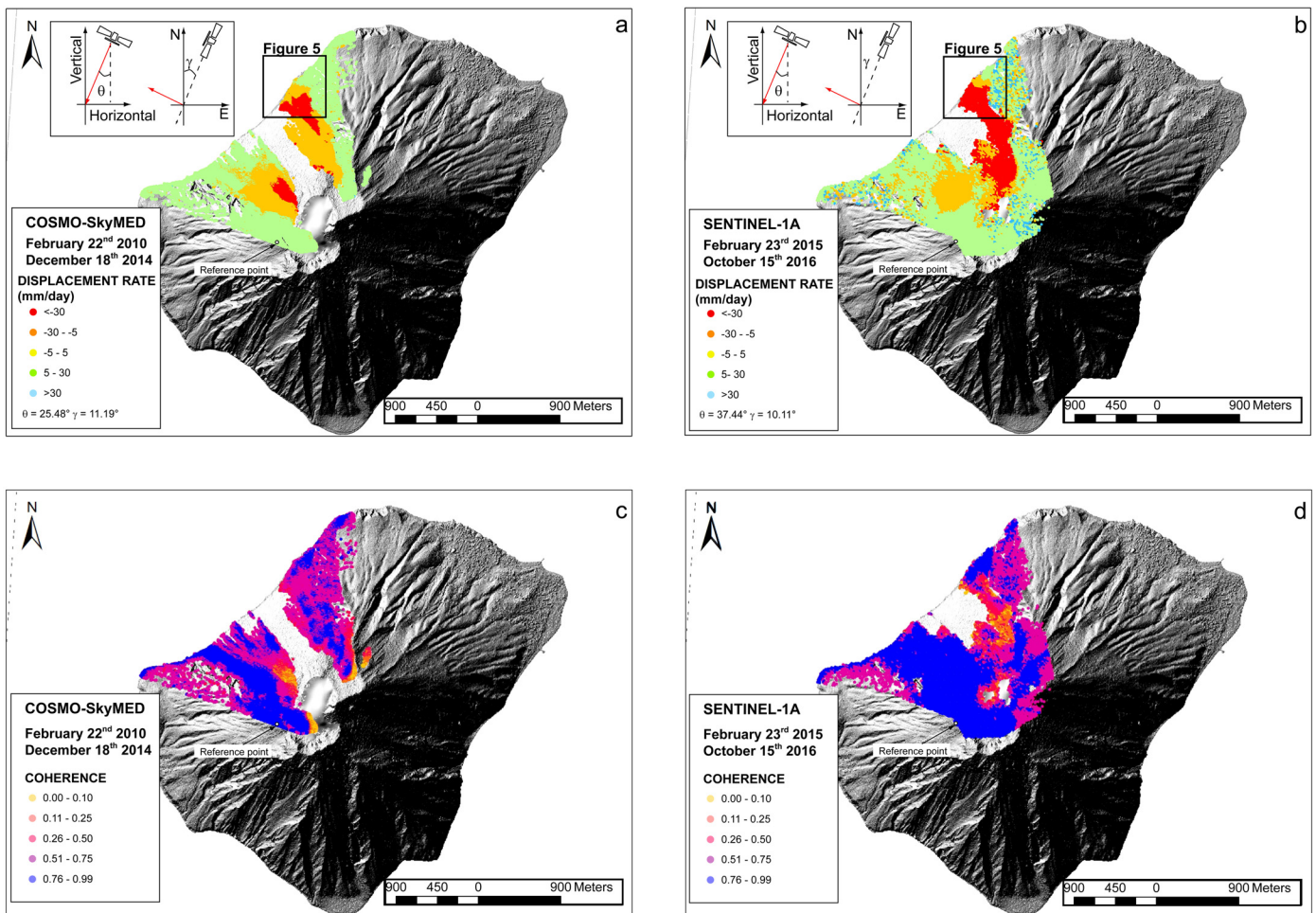
Fig. 2. a) COSMO-SkyMed SqueeSAR™ LOS displacement map (22 February 2010–18 December 2014); b) SENTINEL-1 SqueeSAR™ LOS displacement map (23 February 2015–15 October 2016); c) COSMO-SkyMed SqueeSAR™ LOS coherence map; d) SENTINEL-1 SqueeSAR™ LOS coherence map. The datasets used are in descending orbit (see satellite geometry description in the Supplementary material). (For interpretation of the colours in the figure(s), the reader is referred to the web version of this article.)

very active volcanic islands and volcanic environments because of the frequent ground surface modifications that occur during eruptions and may lead to coherence loss (Dietterich et al., 2012; Di Traglia et al., 2018). Another issue is that of the variability of tropospheric water vapour, which modifies the radar signal (Wadge et al., 2002) and which is a well-known source of noise in repeat-pass interferometry (Hanssen, 2001) that leads to radar delay by causing changes in the refractivity index (Puysségur et al., 2007). This effect is particularly strong along the steep slopes of a volcanic cone, where topographic relief can induce the local flow of air that modifies temperature, pressure, water content, motion and mixing (Kim et al., 2017). Williams et al. (1998) subdivided the procedures needed to reduce tropospheric noise into statistical methods, which exploit a redundant stack of data to limit this component, and calibratory techniques, which measure or model the atmospheric effect by subtracting it from the radar signal. Thus, in this complex environment, it is not always possible to separate deformations from atmospheric noise components without removing and thus underestimating part of the actual deformation. Along the SdF slope, the expected deformations are on the order of several centimetres per year, whereas the atmosphere disturbance is on the order of a few centimetres. For this reason, a slight atmospheric phase screen (APS) filtering was performed (Ferretti et al., 2001), which allowed the preservation of the deformation component as much as possible by losing PS coherence in some sectors of the SdF.

Table 1
FLIR sc620 thermal camera main technical specifications.

Feature	Unit	Value
Detector size	Pixel	640×480
Spectral range	μm	[7.5, 13]
Temperature range	C°	[−40, +500]
Thermal accuracy	C°	±2
Thermal sensitivity	mK	40
Field of view (F.O.V.)	Deg.	24×18
Spatial resolution	m rad	0.65
Minimum focus distance	m	0.3

3.2. Multitemporal infrared thermographic surveys

Several field inspections and multitemporal InfraRed Thermographic (IRT) surveys of the SdF were performed (Fig. 3) in February 2014 (pre-2014 flank eruption), August and September 2014 (syn-2014 flank eruption), and December 2014 (post-2014 flank eruption) in order to analyse the patterns and thermal behaviour of lava flows and their influence on the lava delta, as well as to obtain information about the rock mass fracturing and surface weakness of the lava delta rocks. The IRT surveys were carried out using a handheld FLIR SC620 uncooled microbolometer thermal camera (Table 1; FLIR, 2009). Adjacent thermogram analysis and mosaicking were performed using the FLIR software (FLIR, 2014). A built-in 3.2 Mpixel digital camera, which acquires images in the
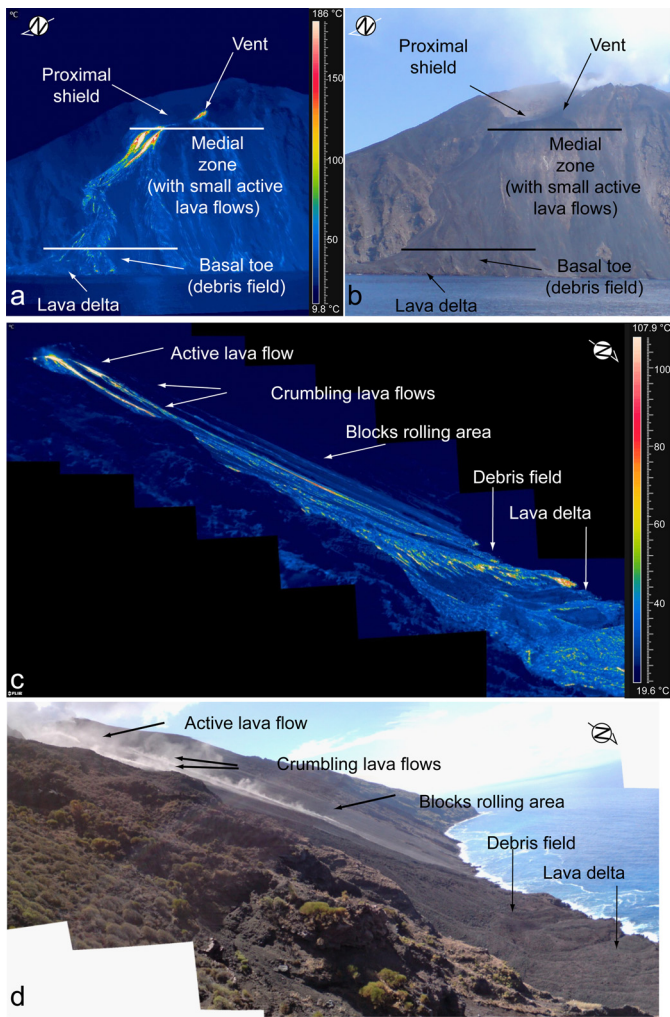
Fig. 3. Multitemporal infrared thermographic (IRT) surveys of the SdF. a) Mosaicked thermograms (with an approximately 52-cm pixel resolution) acquired on 29 August 2014 (15:14 GMT), picturing the front view of the 2014 lava flow field (in the northern sector of the SdF) and the accumulation of hot volcaniclastic material on top of the lava delta; b) corresponding visible scenario; c) mosaicked thermograms (with an approximately 59-cm pixel resolution) acquired on 3 September 2014 (15:40 GMT), enhancing the late 2014 lava flow and its external breccia along the SdF northern sector and the newly formed lava delta; d) corresponding visible scenario images.

visible range simultaneously with respect to the thermograms, improved the interpretation of the detected thermal anomalies.

3.3. Bathymetric survey

To characterize the submerged slope sector of the SdF, a bathymetric survey was carried out in September 2016 (Fig. 4), using a High-Frequency Multibeam (700 KHz UHR frequency; model R2024 of R2Sonic) capable of performing side scan sonar functionalities (TruePix) to determine background morphology. The survey was carried out on-board a 6.9-m-long and 2.4-m-wide catamaran, using the following:

- MBES (MultiBeam Echo-sound System): Multibeam R2 Sonic 2024 depth sounder with a 200–400 kHz transducer;
- DGPS Topcon Legacy-E System and Emisphere V101 Secondary System;
- Motion Sensor integrated with Orion Gyrocompass by TSS-TEledyne;
- QPS QINSy Hydrographic Survey Software.

Given the characteristics of the multibeam system, the seafloor was investigated between −20 and −500 m a.s.l., generating a digital elevation model (DEM) with a cell size of 5 m. Moreover, rockfall hazards from the steep subaerial SdF area prevented us from working close to the coastline. The positioning procedure was performed using a Topcpn Legacy-E model Differential GPS (DGPS) with EGNOSV101 differential correction. The acquisition, management and storage of location and navigation data were performed with a navigation system consisting of a workstation equipped with the QINSy Survey software (produced by QPS). The DGPS surface displacement system was interfaced with all the necessary measurement tools for data acquisition and management. The digital data were organized within a database in a series of files identified by the following parameters: survey line identifier; date of recording; time of recording. The chosen instrumental configuration was designed to optimize all required operations and to simultaneously obtain a high-reliability and precise data set. Details of the bathymetric surveys are reported in the Supplementary Materials.

3.4. 3D limit equilibrium method

The stability of the submarine SdF slope has been evaluated using the Scoops3D software (Reid et al., 2000, 2015). Scoops3D evaluates slope stability with a DEM, using a three-dimensional (3D) method of column approach, which assesses the stability of many potential failure surfaces by considering a user-defined volume range (Reid et al., 2000, 2015). Scoops3D evaluates slope stability using a 3D version of the Bishop's simplified method of limit-equilibrium analysis, considering rotational and spherical landslide surfaces (Reid et al., 2000, 2015).

Scoops3D records the lowest factor of safety (F) for each DEM cell, which is defined as follows:

$$F = \frac{s}{\tau}$$

where τ is the shear stress and s is the shear resistance (strength), which is defined as:

$$s = c + (\sigma_n - u)\tan\varphi$$

where c is cohesion, σ_n is the normal stress, u is the pore–water pressure acting on the shear surface, and φ is the angle of internal friction (Reid et al., 2015). Scoops3D also computes the volume and area associated with each of these potential landslides and determines the least stable potential failure surface for the entire DEM (Reid et al., 2000, 2015). The numerical code also includes the option to represent subsurface materials as full 3D distributions of: i) material cohesion, the angle of internal friction, and weight; ii) earthquake or seismic loading effects in a pseudo-static analysis; iii) pore–water pressure effects, either using pore–pressure ratios (relative to vertical stresses), a piezometric surface or a full 3D distribution of pressure heads; or iv) fully 3D variably saturated groundwater flow fields and the effects of unsaturated suction stresses.

Internal friction and cohesion have sizable effects on the depth of the slip surface and can thus influence the volume and area of a potential landslide (Reid et al., 2015). One way to constrain the influence of the material on the modelled landslide is to use the non-dimensional ratio λ:

$$\lambda = \frac{c}{\gamma H \tan\phi}$$

where c is cohesion, γ is the material unit weight, H is the hillslope height, and ϕ is the angle of internal friction (Janbu, 1955). The higher the λ value, the deeper the critical surface and the
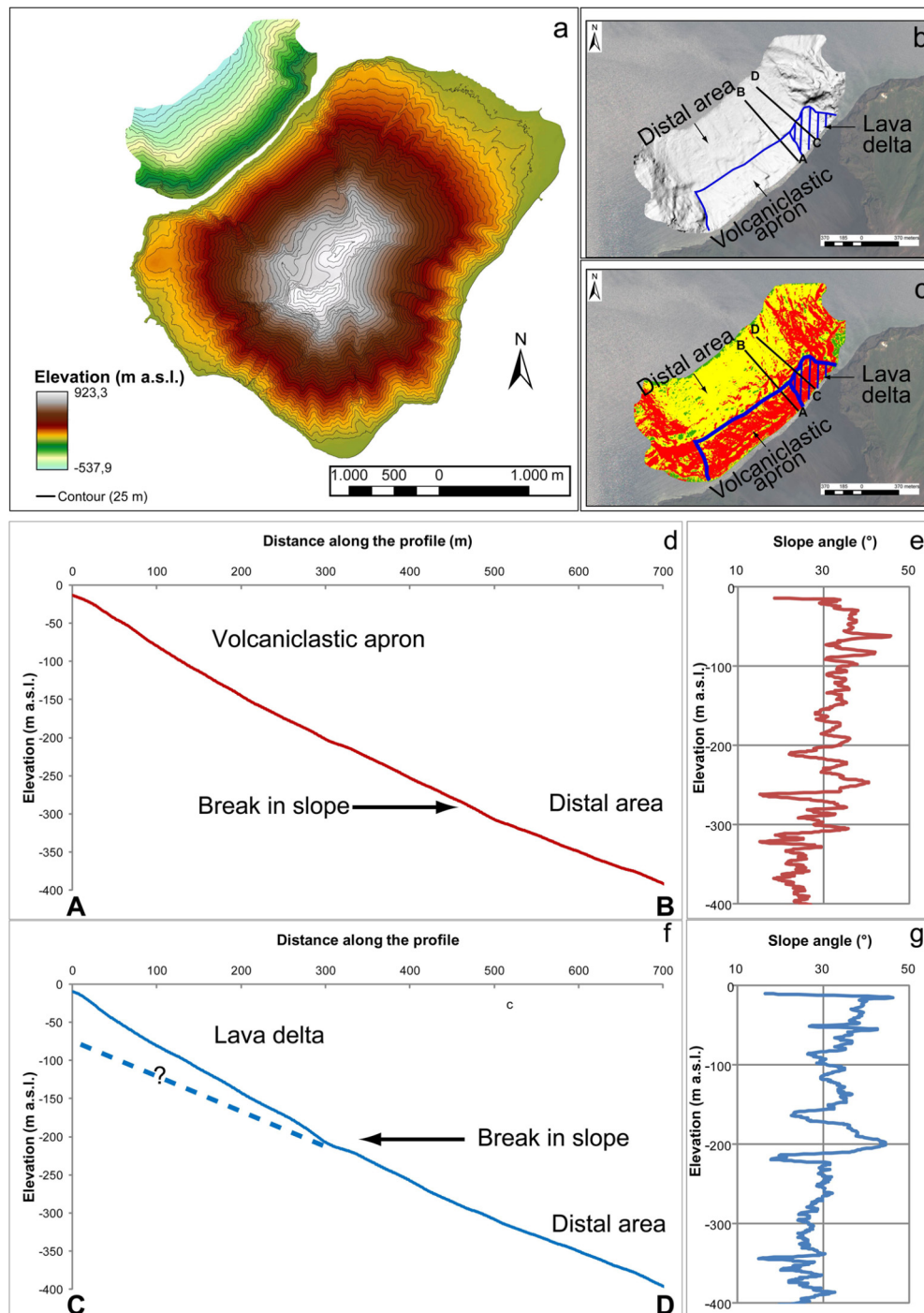
Fig. 4. a) Results of the bathymetric survey (offshore part; see detailed methodology and instrumentation description in the Supplementary material), merged with the relief model derived from a Digital Elevation Model with a pixel resolution of 1×1 m (onshore part) constructed from very high-resolution, panchromatic, tri-stereo images sensed by the Plaieades-1 satellites (collected in May 2016); b) shaded relief model, showing the position of the lava delta with respect to the SdF volcaniclastic apron; c) bathymetric slope angle; d and f) bathymetric profiles; e and g) variations in slope angles with depth. The morphological analysis was used as the starting point of the Limit Equilibrium Analysis model. The volcaniclastic apron and distal area were constructed as a prism comprising a saturated Pyroclastic Deposit Unit (see Table 2), whereas the lava delta was constructed as a prism comprising a saturated Lava Breccia Unit (see Table 2), with thicknesses derived from the bathymetric profiles and variations in the slope angles with depth.

larger the associated volume. For $\lambda = 0$, the critical surface is always shallow, with the smallest volume.

Based on submarine morphology and previous reconstructions (Kokelaar and Romagnoli, 1995; Chiocci et al., 2008a, 2008b; Casalbore et al., 2010; Bosman et al., 2014), the LEM analysis was constructed considering two layers of subsurface materials, namely, i) volcaniclastic deposits, which comprise the entire submarine SdF

slope; and ii) the lava delta that covers the volcaniclastic deposits in the northernmost region of the SdF, which extends from the coastline to approximately -250 m a.s.l. Because the aim was to model only the effect of the lava delta on the stability of the SdF volcaniclastic apron, the lateral SdF edges were not considered. The water table was assumed to be flat and coincident with sea level, representing the vertically hydrostatic pressure heads beneath the

Table 2
Material properties assigned to the 3D model with the Limit Equilibrium Method. Data from Boldini et al. (2009), Rotonda et al. (2009) and Nolesini et al. (2013).

Layer	Unit	Cohesion (kPa)	Friction angle (°)	Dry unit weight (kN/m³)	Saturated unit weight (kN/m³)
Lava delta	Lava-Breccia	30	35	20.76	22.90
Volcaniclastic apron and distal area	Pyroclastic deposits	600	23	17.16	19.62

surface (i.e., the water load on the slope). The pore pressure acting on the slope is defined by the vertical depth beneath the piezometric surface multiplied by the unit weight of water (Reid et al., 2015). The pore pressure, u, is related to the pressure head, h (in units of length), and the water unit weight, γ_w, by the following equation:

$$u = h\gamma_w$$

The unit weight (γ_s), angle of internal friction and cohesion of the saturated SdF material (Boldini et al., 2009; Nolesini et al., 2013) are used to determine the potential failure mass beneath the piezometric surface (Table 2).

4. Results

4.1. Ground deformation maps

Within the entire SdF area, the SqueeSAR analysis of the CSK dataset revealed that the maximum displacement recorded in the SdF sector is related to the presence of the 2007 and 2014 lava flow fields in the northern SdF and that of the 2010 and 2011 overflows in the western SdF (overflows are reported in Fig. 1d and related displacement in Fig. 2a), whereas the maximum displacement recorded by the SNT dataset is only related to the presence of the 2014 lava flow field (Fig. 2b).

Ground displacement maps revealed the differential ground motion of the lava delta in both the CSK and SNT datasets, identifying a stable area in the northern SdF and an unstable area in the central SdF (Fig. 5a, b). The northern part of the delta is stable in both datasets (yielding velocities of less than 2 mm/y), whereas the central part (between points 1–2 and points 5–6 for CSK and SNT datasets, respectively – Fig. 5a, b) is characterized by average displacement rates on the order of 30 mm/y and 160 mm/y for the CSK and SNT datasets, respectively.

4.2. Time series analysis

The analysis of the profile tracks (Fig. 5c, d) and displacement time series extracted from single DS located along them (Fig. 5e, f) confirmed the differential ground motion of the delta. The unstable portion records high displacement values since 2010, reaching cumulative values of 200 mm in the period between 2010–2014 for the CSK dataset and between 2015–2016 for the SNT dataset, for a total amount of more than 400 mm between February 2010 and October 2016. The CSK time series of deformation for Points 1, 2 and 3 show a clear change in trend in the last part of the series, corresponding to the 2 December 2014 acquisition. The registered acceleration is equal to 70 mm/yr for Point 1 and 20 mm/yr for Points 2 and 3. The SNT time series shows another change in trend during the 2016 as highlighted by the time series of Points 5 and 6, located in the central sector of the lava delta, which register a strong deceleration starting from the April 2016 acquisitions, when the deformation velocities drop from 180 mm/yr and 70 mm/yr for Points 5 and 6, respectively toward the stability. Point 7, which is located at the boundary with the delta stable sector and Point 8, which is located within the stable area, registers minor temporal oscillations of displacement values (i.e. around November 2015 and August 2016). These variations are not connected to a ground surface process but are most likely related to the intrinsic variation, of

few millimetres for each acquisition, of the PSI processing and thus of the derived time series. The no-data zones, which are located in both datasets within the central SdF area (Fig. 2), are consistent with the accumulation of volcaniclastic material, mainly derived from Strombolian activity at the summit crater terrace (Di Traglia et al., 2018). This dynamic landscape evolution produces very low coherence, thus precluding any possible measurement of the displacements using the SqueeSAR technique (Di Traglia et al., 2018).

A first-order investigation of the relationship between the lava delta subsidence and the thickness of the 2014 lava flow was carried out using two Digital Elevation Models (DEMs; Fig. 5d) that were collected in 2012 and 2017. The 2012 DEM was obtained using airborne laser scanning (xy resolution: 0.5×0.5 m; z resolution: 1 m; the same used by Di Traglia et al. (2018), whereas the 2016 DEM was obtained using very high-resolution (VHR) tri-stereo optical imagery from the PLEIADES-1 satellites (xy resolution: 1×1 m; z resolution: 2.5 m). As can be observed in Fig. 5d, there is no direct correlation between the thickness of the 2014 lava flow and the displacement values measured in the SNT dataset.

4.3. Multitemporal infrared thermography

The IRT survey (Fig. 3) revealed the typical Stromboli lava flow field morphology produced by a high-elevation vent (as described for the 2002–2003 lava flow field by Lodato et al., 2007), which comprised i) a proximal shield, formed by a series of tumuli and their resultant 'a'a flows around the effusive vent at ≈650 m a.s.l.; ii) a medial zone fed by small flows (large flows were emplaced only during the initial high-effusion-rate phase – 7–10 August 2014) and characterized by steep slopes that caused both lava crumbling (Fig. 3c, d) and the production of a debris field; iii) a basal toe composed of the debris flow field emplaced above the stacked lava delta, comprising the 2007 and early (7–10 August 2014) lava flows. The IRT inspections also revealed the rapid cooling of the lava delta, as it was no longer fed directly by lava flows after the first 3–4 days following the eruption's onset. During the field surveys, no evidence of fracturing processes related to instability phenomena were observed.

4.4. Bathymetric survey

From the isobaths shape (Fig. 4a), it is immediately possible to notice the absence of the 30 December 2002 landslide scar (with a max. depth of 45 m and a max. width of 650 m, located in the northern edge of the SdF sub-marine part; Fig. 1c), thus accounting for an almost complete scar filling, as was observed by Chiocci et al. (2008a). A slope versus depth analysis, based on the new bathymetric reconstruction, allowed the identification of two different sectors of the surveyed part of the submerged SdF (Fig. 4e, g): i) a proximal area (from the coastline to −250–−300 m a.s.l.), which is characterized by a steeper slope (>30°) and a smoother morphology, definable as a volcaniclastic fan-deltoid apron (Casalbore et al., 2010); ii) the lava delta, which is located in the northern part of the proximal area, showing a slope gradient of >40° and a rough surface; iii) a distal area, deeper than −300 m a.s.l., with a slope gradient of <30° and a smooth morphology.
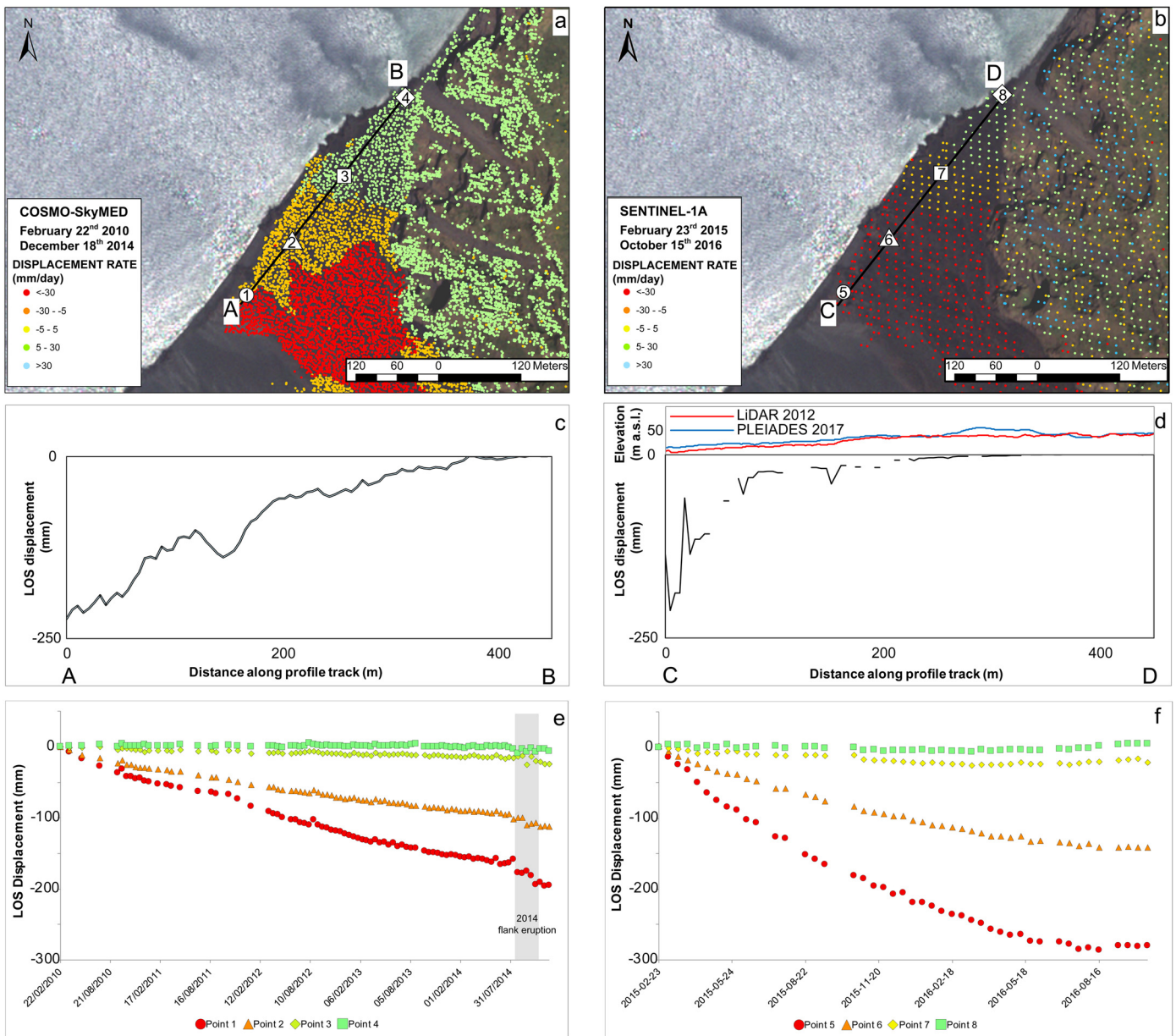
Fig. 5. Details of the lava delta area: a) COSMO-SkyMed SqueeSAR LOS displacement map (22 February 2010–18 December 2014) and b) SENTINEL-1 SqueeSAR LOS displacement map (23 February 2015–15 October 2016); c) displacement trend along the profile tracks recorded by processing COSMO-SkyMed images; d) topographic profiles collected in 2012 (*xy* resolution: 0.5 × 0.5 m; *z* resolution: 1 m) and 2017 (PLEIADES-1; *xy* resolution: 1 × 1 m; *z* resolution: 2.5 m) were also reported, highlighting the absence of any relationship between the thickness of the lava accumulated in 2014 and the observed displacements; e) displacement trend along the profile tracks recorded by processing SENTINEL-1A images; f) displacement time series measured in the points evidenced in a) tracks recorded by processing COSMO-SkyMed images; g) displacement time series measured in the points evidenced in b) recorded by processing SENTINEL-1A images. The location of points 1, 2, 3 and 4 are the same of those of points 5, 6, 7 and 8 respectively.

Table 3
Model results.

Search volume interval (m³)	Lowest F	Volume with lowest F ($\times 10^6$ m³)	Area with lowest F ($\times 10^5$ m²)	Max thickness with lowest F (m)	Volume with $F < 1$ ($\times 10^6$ m³)
10^5–10^6 m³	0.93	0.9×10^6	1.3	29	9.97
10^6–10^7 m³	0.83	8.59×10^6	5.2	50	9.99
10^7–10^8 m³	0.83	11.2×10^6	5.9	52	2.3

4.5. 3D limit equilibrium method

The stability analysis was conducted using three different ranges of landslide volumes (Table 3), considering small (10^5–10^6 m³) to moderate (10^6–10^7 m³) to large (10^7–10^8 m³) submarine slope failures. F values between 0.9 and 1.1 always

characterized the submarine slope between the coastline and -250 m a.s.l. for all simulations, while higher values are observed in distal areas (Fig. 6). The critical surface with the lowest factor of safety ($F = 0.93$) for small-volume simulations involves much of the lava delta at depths between -5 and -260 m or -250 m a.s.l. (Fig. 6a). The resulting potential landslide has a volume of
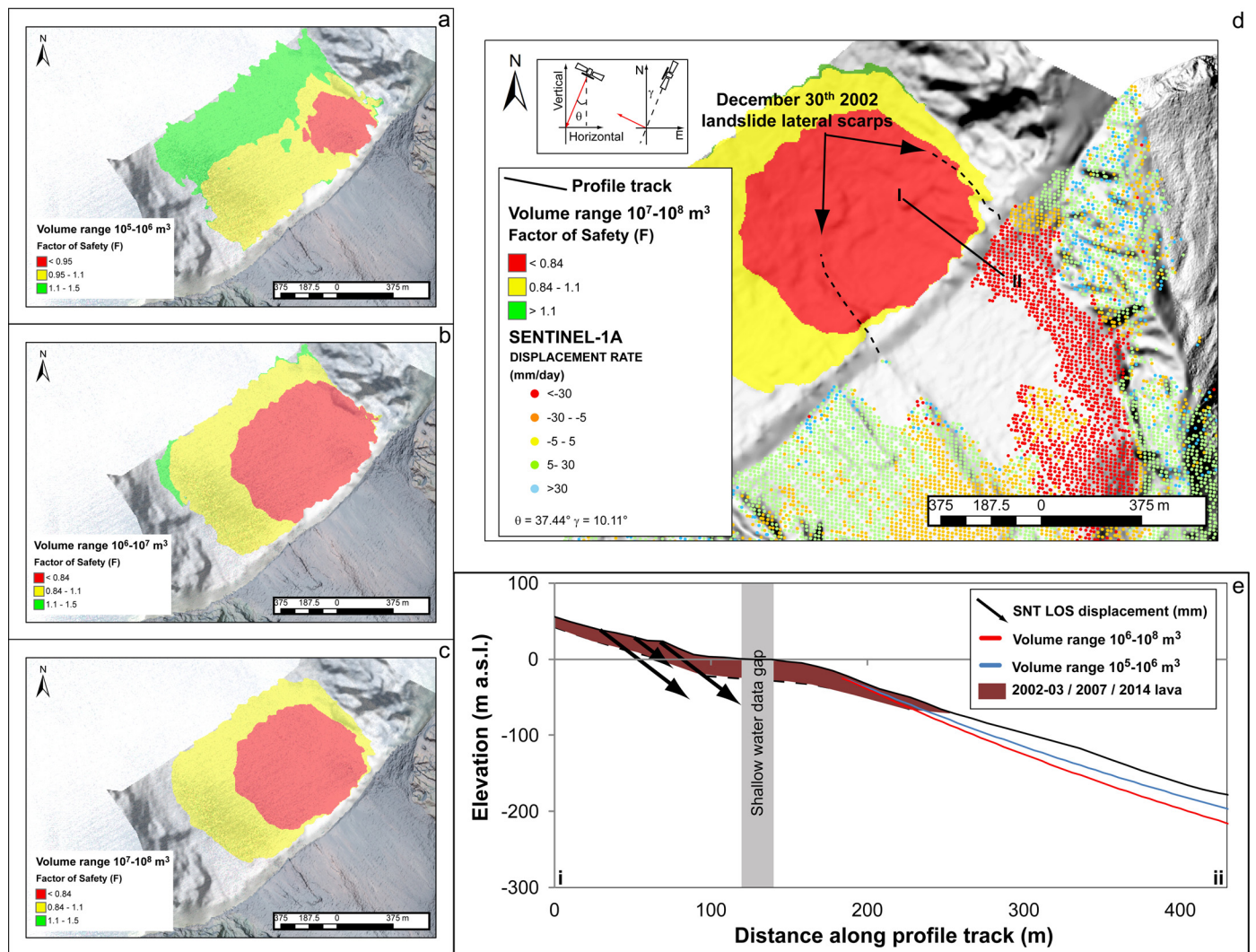
Fig. 6. Limit Equilibrium Analysis results for different landslide search volumes: a) volumes ranging from 10^5–10^6 m^3; b) volumes ranging from 10^6–10^7 m^3; c) volumes ranging from 10^7–10^8 m^3; d) comparison between the Limit Equilibrium Models results (with search volumes ranging from 10^7–10^8 m^3) and the SENTINEL-1 SqueeSAR™ LOS displacement map (23 February 2015–15 October 2016), highlighting the limit of the 30 December 2002 τ slide reported by Chiocci et al. (2008a). In a), b), c), and d) the lower F values (0.84, 0.95, 0.95) represent the lowest finding of the stability modelling for each search volume interval. In e) the displacement and LEM results along the profile track I–II is shown.

0.9×10^6 m^3, with a maximum thickness of 29 m and an area of 1.3×10^5 m^2. In the second set of analyses, the critical surface ($F = 0.83$) is located in the central area of SdF, involving part of the lava delta, at depths between -20 and -400 m a.s.l. (Fig. 6b). The resulting potential landslide has a volume of 8.59×10^6 m^3, with a maximum thickness of $\sim$50 m and a sliding surface of 5.2×10^5 m^2. The largest potential landslide ($F = 0.83$) has been identified in the central area of SdF, in the same position as the moderate-volume landslides, at depths between -20 and -420 m a.s.l. (Fig. 6c). It has a volume of 11.2×10^6 m^3, with a maximum thickness of 52 m and a sliding surface of 5.9×10^5 m^2 (Table 3).

5. Discussion

SAR instruments can detect post-emplacement lava flow motions related to different mechanisms (Stevens et al., 2001): i) thermal contraction (movements perpendicular to the pre-effusive slope; Fig. 7a); ii) the readjustment of external breccia, resulting in radar phase decorrelation due to the rapid and chaotic movement of surface scatterers (e.g. Dietterich et al., 2012; Fig. 7b); and iii) the time-dependent depression the substrate triggered by overloading, affecting the area covered by the newly emplaced

material and a margin extending some tens to hundreds of metres beyond it (Stevens et al., 2001; Chen et al., 2017). On flat topography, this latter effect will produce vertical movements (Stevens et al., 2001), which will turn into slope instability (down-slope movements) on steep slope topography (Fig. 7c; (Bonforte et al., 2016; Di Traglia et al., 2018). Other SAR signals associated with the subsidence of lava flows gravity-driven slip or landsliding (e.g., Ebmeier et al., 2014). Moreover, the thermal-induced fracturing of the lava flow (joint formation) could increase down-slope movements on steep slope topography (Fig. 7a). In the case of lava deltas, ground deformation is generally attributed to the thermal contraction of cooling lava and the compaction of volcaniclastic materials (i.e., pre-existing deposits and autoclastic debris) below the delta itself (Poland and Orr, 2014). On Stromboli, SAR coherence is reduced only in localized areas placed upslope with respect to the lava delta, implying that the readjustment of the external breccia makes only a small contribution to the InSAR signal (Fig. 7b). In the delta area, the overall coherence remained at high values ($>$0.5) for both datasets (Fig. 2c, d). The crumbling of newly emplaced 2014 lava and breccia movement along the slope, as highlighted by the IRT surveys (Fig. 3), was measured by Di Traglia et al. (2018) using a ground-based InSAR apparatus.
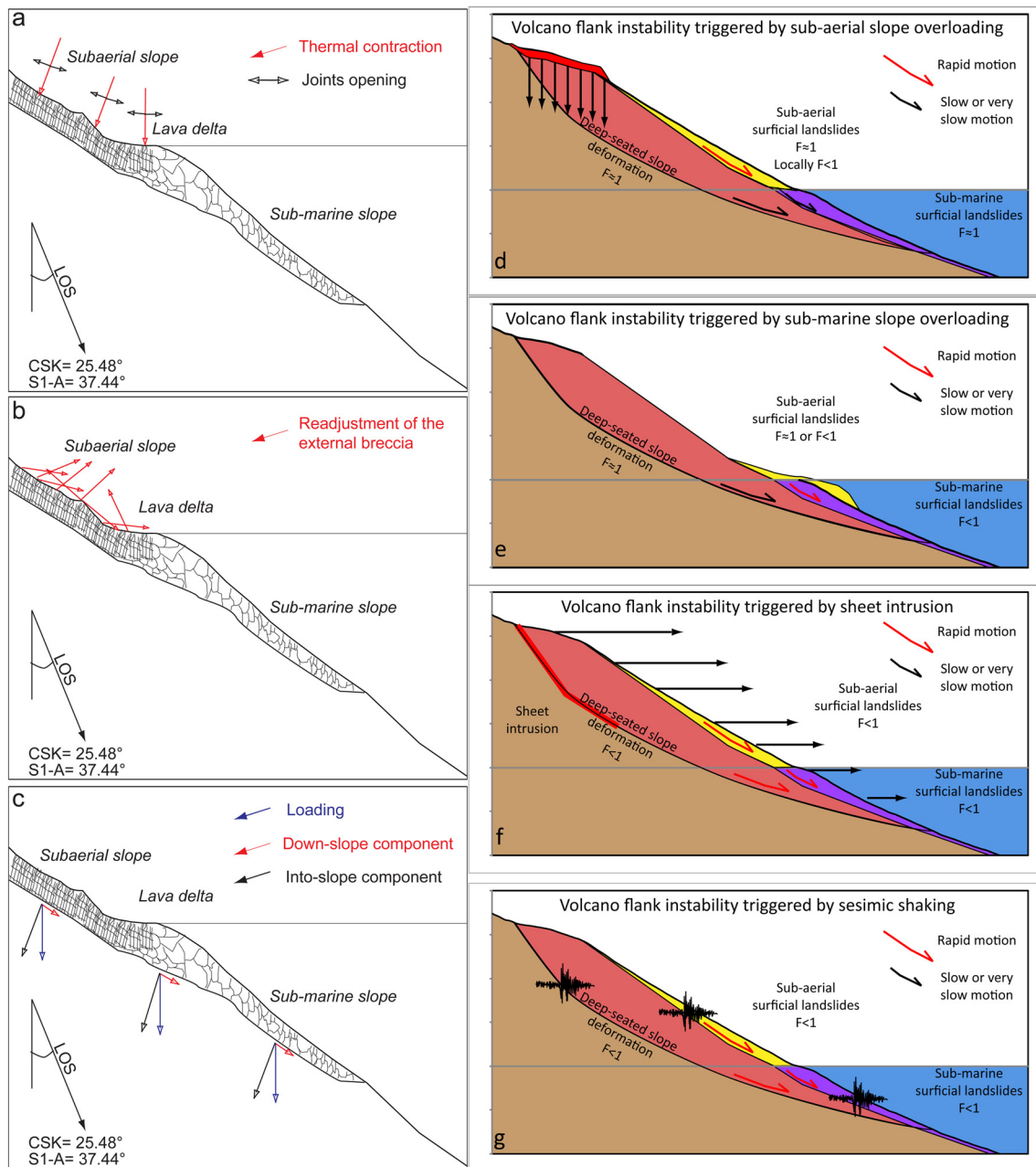
Fig. 7. In a), b) and c) the conceptual model for post-emplacement lava flow motions related to different components is shown: a) thermal contraction (movements perpendicular to the pre-effusive slope) and thermal-induced joint formation (down-slope movements on steep slope topography); b) readjustment of the external breccia, resulting in low coherence in the radar phase due to the rapid and chaotic movement of surface scatterers; iii) the time-dependent depression of the substrate triggered by overloading, affecting the area covered by newly emplaced material and a margin extending some tens to hundreds of metres beyond it, thus increasing the slope instability (down-slope movements) on steep slope topography. The LOS direction is a simplified scheme that can be used by the reader to understand the acquisition geometry (see satellite geometry description in the Supplementary material). The section is oriented along the LOS direction, representing the most suitable situation for a InSAR based monitoring study and it is only a conceptual model of the phenomena that occur during the lava emplacement and the radar response of the slope in terms of ground deformation. In order to correctly estimate the E–W and N–S components, it is mandatory to combine both ascending and descending orbits (Bonforte et al., 2011). Unfortunately, the data reported here have been processed only in one orbit, that is the effettive for limiting shadowing and layover problems on the Sciara del Fuoco slope. In d), e), f), and g) the conceptual model for the main triggers of volcanoes slope instability is shown. The motion of the surficial material ($F < 1$ condition), without the involvement of the deep-seated landslide ($F \approx 1$ condition), can be triggered by slope overloading in the d) sub-aerial part (as occurring at Stromboli after the 2014 flank eruption; Di Traglia et al., 2018), or e) in the sub-marine part (as during the lava delta collapse at Kilauea; Sansone and Smith, 2006). Other mechanisms, f) like sheet intrusion (as occurred at Stromboli during the 2002–2003 flank eruption; Bonaccorso et al., 2003) and g) seismic shaking can trigger the destabilization of the entire volcano flank (Voight and Elsworth, 1997), reducing the factor of safety at shallower and deeper levels.

The same movements were impossible to measure by applying the SqueeSAR technique to CSK imagery, due to the satellite revisiting time (16 days during the 2014 flank eruption). IRT and field inspections also showed the rapid cooling of the lava delta and no evidence of fracturing processes related to instability phenomena (Fig. 3).

This work is focused on the effect of the slope loading to the shallow motion of surficial deposits (see Nolesini et al., 2013 for the modelling, comparison with GBInSAR data and discussion), not considering deep-seated, persistent flank motion ("volcanic spreading", see Poland et al., 2017). LEM analyses highlighted that the high-gradient proximal area is characterized by low F val-

ues (0.9–1.1) relative to more distal areas (Fig. 6). Moreover, the lowest F value for each search volume is always located in the volcaniclastic apron around the lava delta, in the same position as the 30 December 2002 landslide. This likely reflects the beginning of a new instability phase like that which occurred before the 30 December 2002 tsunamigenic landslide. It is worth noting that the northernmost part of the lava delta overlies the northern, stable, SdF lateral margin (Chiocci et al., 2008b). The measured displacement may be related to the instability of the volcaniclastic apron within the 2002 scar due to the low strain rate likely associated with the loading of the volcaniclastic material exerted by the lava delta under drained conditions (Fig. 6e), which implies that the drained shear strength of the SdF volcaniclastic infill is higher than the maximum shear stress related to delta loading. This theory is also supported by the time series of deformation extracted from the CSK dataset in the moving sector of the lava delta, where an abrupt acceleration, which is directly connected to the emplacement of the lava flows during the 2014 eruption, which began in August 2014, was registered (Fig. 5e and f). In the stable sector of the lava delta, the time series of deformation showed only minor-order oscillations, confirming the correlation between the displacements registered with the underwater morphology and the lithology of the lava delta. If the shear rate increases, the undrained load conditions could generate a liquefied flow (Chiocci et al., 2008a). Shear-rate intensification could be related to the reactivation of deep-seated gravitational slope deformations (α slide), as proposed by Chiocci et al. (2008a) for the 30 December 2002 event, or by slope overloading from a subaerial landslide, as proposed by Nolesini et al. (2013).

Lava delta instability has been measured at Pico Island (Azores; Hildenbrand et al., 2012) and Kilauea volcano (Hawaii; Poland and Orr, 2014). At the latter location, InSAR data Revealed that lava delta instability (seaward displacement and subsidence) occurred at more than 5 mm/day and ended after complete collapse of the delta (Poland and Orr, 2014). In the first case, the slump of the southeastern flank of Pico Island has been identified. The slump, involving several cubic kilometres of the subaerial and submarine volcano structure, shows little horizontal displacement (1.6 ± 1.3 mm/yr), but significant (5–12 mm/yr) downward movement (Hildenbrand et al., 2012). The lava deltas mentioned earlier in the text were emplaced in areas affected by large scale flank deformation but only Stromboli and Pico instabilities registered the same velocity magnitude of surrounding slope, while the Kilauea deltas show higher velocity compared to the so called Hilina slump (Poland et al., 2017 for a review on Kilauea flank instability). Generally speaking, moving lava deltas can be considered as landslides. In the case of Stromboli, the new lava delta filled the 30 December 2002 landslide scar, and InSAR measures a subsidence at a rate in the order of 10^1–10^2 mm/yr. In this case, as also in the case of the Pico subaerial–submarine slump, it can be classified as a very slow landslide, in terms of Cruden and Varnes (1996) classification. At Kilauea, rapid mass wasting of shallow submarine basalts was documented in 1990 (Sansone and Smith, 2006). Effusive eruption produced the widespread formation of lava pillows at this site over a water depth range of 20–40 m, that collapsed over few days generating a debris field composed of material ranging in size from fine sand to boulder fragments (Sansone and Smith, 2006). In this case, the pre-collapse data can be used to classify the delta movements as slow landslides moving within the perimeter of a bigger, very slow landslide (HIlina slump). The continuous down-slope motion of these slopes (and deltas) implies a limit equilibrium condition for the volcano flanks (i.e. the factors of safety approach the unity). In all cases, an acceleration of the system caused by slope overload (Kilauea collapses; Sansone and Smith, 2006) or other types of forcing (dike intrusion, overloading, seismic shaking, etc.), can produce a strong increase in velocity

(sudden drop in F) and the development of rapid flow-like landslides (debris flow/avalanches and/or turbidites; Hutchinson, 1986).

6. Conclusions

Slope failures of volcanic edifices produce a wide spectrum of instability phenomena, from small rock-falls to large-scale slope deformation, eventually evolving in rock-slides or debris avalanches. The greatest danger associated with landslides in coastal or on island volcanoes is their ability to generate tsunamis whose effects can propagate far away from the source areas. In addition, the coastal population is progressively increasing all over the world, thus the danger caused by tsunamigenic landslides is expected to grow in the future.

Our efforts have focused on Stromboli volcano, an optimal environmental setting and a case history of volcano slope instability phenomena, since: i) it experienced moderate to major instability events, ii) its slopes are prone to mass-wasting phenomena, iii) recent flank eruptions produced a stacked lava delta that can be monitored using remote sensing techniques; iv) its flanks are affected by persistent volcanic activity that can significantly affect the stability of slopes, v) landslides from its flanks may generate tsunamis that could affect inhabited areas, and vi) it is one of the best studied and, among all, monitored volcano on Earth, providing exceptional validation data and ground-truth constrains. In this study, X-band COSMO-SkyMED and C-band SENTINEL-1 SAR images, obtained from February 2010 to October 2016, were processed using the SqueeSAR algorithm. Moreover, a 3D Limit Equilibrium Method (LEM) analysis was constructed based on new underwater data. In more detail:

- SqueeSAR data revealed differential ground motion of the lava delta in both the CSK and SNT datasets, identifying a stable area in the northern SdF and an unstable area in the central SdF;
- The displacement time series confirmed this internal delta subdivision, which also demonstrated the presence of abrupt changes in the trends in the unstable portion of the SdF that were connected to the emplacement of the 2014 eruption lava flows;
- The boundary between the two areas corresponds to the northern edge of the 30 December 2002 tsunamigenic landslides;
- the Factor of Safety (F) ranges from 0.9 to 1.1 between the coastline and -250 m a.s.l. for all simulations;
- The lowest factor of safety for all search volumes always involves the greater part of the lava delta and matches the 30 December 2002 landslide boundary;
- The resulting potential landslides range in volume from 0.9×10^6 m^3 to 11.2×10^6 m^3, with maximum thicknesses ranging from 29 m to 52 m;
- The measured InSAR-derived displacement can be related to the sliding of volcaniclastic materials due to the lava delta load under drained conditions (i.e., the drained shear strength of the SdF infill is higher than the maximum shear stress related to delta loading).

Comparing data from Stromboli with ground displacement measurements at Pico Island and Kilauea volcano, it is possible to state that lava delta motion is the evidence of the instability phenomena that take place in the flanks of the volcanoes. The continuous down-slope motion of the volcano slopes (and deltas) implies a limit equilibrium condition for the slopes. Any kind of perturbation that leads to an acceleration of the system, can produce a strong increase in the ground velocity and the development of rapid flow-like landslides. The successful strategy proposed here

combines field-based observations and advanced techniques, such as remote sensing and numerical modelling, to provide information about both the nature and the extent of the post-effusive deformation field and the cause of the detected lava delta deformation. This study demonstrates how MT-InSAR techniques support the detection of lava delta instabilities and the identification and monitoring of coastal or submarine landslides in volcanic setting.

Acknowledgements

Appendix A. Supplementary material

Supplementary material related to this article can be found online at https://doi.org/10.1016/j.epsl.2018.01.038.

References

Boldini, D., Wang, F., Sassa, K., Tommasi, P., 2009. Application of large-scale ring shear tests to the analysis of tsunamigenic landslides at the Stromboli volcano, Italy. Landslides 6 (3), 231–240.

Bonaccorso, A., Calvari, S., Garfì, G., Lodato, L., Patanè, D., 2003. Dynamics of the December 2002 flank failure and tsunami at Stromboli volcano inferred by volcanological and geophysical observations. Geophys. Res. Lett. 30 (18). SDE 6-1–6-4.

Bonforte, A., González, P.J., Fernández, J., 2016. Joint terrestrial and aerial measurements to study ground deformation: application to the Sciara Del Fuoco at the Stromboli Volcano (Sicily). Remote Sens. 8 (6), 463.

Bonforte, A., Guglielmino, F., Coltelli, M., Ferretti, A., Puglisi, G., 2011. Structural assessment of Mount Etna volcano from Permanent Scatterers analysis. Geochem. Geophys. Geosyst. 12 (2), 1–12.

Bosman, A., Casalbore, D., Romagnoli, C., Chiocci, F.L., 2014. Formation of an 'a'ā lava delta: insights from time-lapse multibeam bathymetry and direct observations during the Stromboli 2007 eruption. Bull. Volcanol. 76 (7), 838.

Calvari, S., Bonaccorso, A., Madonia, P., Neri, M., Liuzzo, M., Salerno, G.G., Behncke, B., Caltabiano, T., Cristaldi, A., Giuffrida, G., La Spina, A., Marotta, E., Ricci, T., Spampinato, L., 2014. Major eruptive style changes induced by structural modifications of a shallow conduit system: the 2007–2012 Stromboli case. Bull. Volcanol. 76 (7), 1–13.

Calvari, S., Spampinato, L., Lodato, L., Harris, A.J., Patrick, M.R., Dehn, J., Burton, M., Andronico, D., 2005. Chronology and complex volcanic processes during the 2002–2003 flank eruption at Stromboli volcano (Italy) reconstructed from direct observations and surveys with a handheld thermal camera. J. Geophys. Res., Solid Earth 110 (B2), 1–23.

Casalbore, D., Romagnoli, C., Chiocci, F., Frezza, V., 2010. Morpho-sedimentary characteristics of the volcaniclastic apron around Stromboli volcano (Italy). Mar. Geol. 269 (3), 132–148.

Chen, Y., Remy, D., Froger, J.L., Peltier, A., Villeneuve, N., Darrozes, J., et al., 2017. Long-term ground displacement observations using InSAR and GNSS at Piton de la Fournaise volcano between 2009 and 2014. Remote Sens. Environ. 194, 230–247.

Chiocci, F.L., Romagnoli, C., Bosman, A., 2008b. Morphologic resilience and depositional processes due to the rapid evolution of the submerged Sciara del Fuoco (Stromboli Island) after the December 2002 submarine slide and tsunami. Geomorphology 100 (3), 356–365.

Chiocci, F.L., Romagnoli, C., Tommasi, P., Bosman, A., 2008a. The Stromboli 2002 tsunamigenic submarine slide: characteristics and possible failure mechanisms. J. Geophys. Res., Solid Earth 113 (B10), 79–89.

Crosetto, M., Monserrat, O., Cuevas-González, M., Devanthéry, N., Crippa, B., 2016. Persistent scatterer interferometry: a review. ISPRS J. Photogramm. Remote Sens. 115, 78–89.

Cruden, D.M., Varnes, D.J., 1996. Landslide types and processes. In: Turner, A.K., Schuster, R.L. (Eds.), Landslides Investigation and Mitigation. Special Report 247. Transportation Research Board, US National Research Council, Washington, DC, pp. 36–75 (Chapter 3).

Di Roberto, A., Rosi, M., Bertagnini, A., Marani, M.P., Gamberi, F., 2010. Distal turbidites and tsunamigenic landslides of Stromboli volcano (Aeolian Islands, Italy). In: Submarine Mass Movements and Their Consequences. Springer, Dordrecht, pp. 719–731.

Di Traglia, F., Nolesini, T., Ciampalini, A., Solari, L., Frodella, W., Bellotti, F., Fumagalli, A., De Rosa, G., Casagli, N., 2018. Tracking morphological changes and slope instability using spaceborne and ground-based SAR data. Geomorphology 300, 95–112.

Dietterich, H.R., Poland, M.P., Schmidt, D.A., Cashman, K.V., Sherrod, D.R., Espinosa, A.K., 2012. Tracking lava flow emplacement on the east rift zone of Kilauea Hawai'i, with synthetic aperture radar coherence. Geochem. Geophys. Geosyst. 13, Q05001. https://doi.org/10.1029/2011GC004016.

Ebmeier, S.K., Biggs, J., Muller, C., Avard, G., 2014. Thin-skinned mass-wasting responsible for widespread deformation at Arenal volcano. Earth Sci. Front. https://doi.org/10.3389/feart.2014.00035.

Ferretti, A., Fumagalli, A., Novali, F., Prati, C., Rocca, F., Rucci, A., 2011. A new algorithm for processing interferometric data-stacks: SqueeSAR. IEEE Trans. Geosci. Remote Sens. 49 (9), 3460–3470.

Ferretti, A., Prati, C., Rocca, F., 1999. Permanent scatterers in SAR interferometry. In: IEEE 1999 International Geoscience and Remote Sensing Symposium, IGARSS'99 Proceedings, vol. 3. IEEE, pp. 1528–1530.

Ferretti, A., Prati, C., Rocca, F., 2001. Permanent scatterers in SAR interferometry. IEEE Trans. Geosci. Remote Sens. 39 (1), 8–20.

FLIR, 2009. FLIR ThermaCAM SC620 technical specifications. http://www.flir.com/cs/emea/en/view/?id=41965.

FLIR, 2014. FLIR ResearchIR 3.4. sp3. http://support.flir.com/DsDownload/Assets/T198206_en_40.pdf.

Hanssen, R.F., 2001. Radar Interferometry: Data Interpretation and Error Analysis, vol. 2. Springer Science & Business Media.

Hildenbrand, A., Marques, F.O., Catalão, J., Catita, C.M.S., Costa, A.C.G., 2012. Large-scale active slump of the southeastern flank of Pico Island, Azores. Geology 40 (10), 939–942.

Hooper, A., Zebker, H.A., 2007. Phase unwrapping in three dimensions with application to InSAR time series. J. Opt. Soc. Am. A 24 (9), 2737–2747.

Hutchinson, J.N., 1986. A sliding–consolidation model for flow slides. Can. Geotech. J. 23 (2), 115–126.

Janbu, N., 1955. Application of composite slip surfaces for stability analysis. In: European Conference on Stability of Earth Slopes, vol. 3, pp. 43–49.

Jurado-Chichay, Z., Rowland, S.K., Walker, G.P., 1996. The formation of circular littoral cones from tube-fed pāhoehoe: Mauna Loa, Hawai'i. Bull. Volcanol. 57 (7), 471–482.

Kim, J.R., Lin, S.Y., Yun, H.W., Tsai, Y.L., Seo, H.J., Hong, S., Choi, Y., 2017. Investigation of potential volcanic risk from Mt. Baekdu by DInSAR time series analysis and atmospheric correction. Remote Sens. 9 (2), 138.

Kokelaar, P., Romagnoli, C., 1995. Sector collapse, sedimentation and clast population evolution at an active island-arc volcano: Stromboli, Italy. Bull. Volcanol. 57 (4), 240–262.

Kwam, P., Vidakovic, B., 2007. Nonparametric Statistics with Applications to Science and Engineering. Wiley, Hoboken, NJ.

Lipman, P.W., Moore, J.G., 1996. Mauna Loa lava accumulation rates at the Hilo drill site: formation of lava deltas during a period of declining overall volcanic growth. J. Geophys. Res., Solid Earth 101 (B5), 11631–11641.

Lodato, L., Spampinato, L., Harris, A., Calvari, S., Dehn, J., Patrick, M., 2007. The morphology and evolution of the Stromboli 2002–2003 lava flow field: an example of a basaltic flow field emplaced on a steep slope. Bull. Volcanol. 69 (6), 661–679.

Marsella, M., Baldi, P., Coltelli, M., Fabris, M., 2012. The morphological evolution of the Sciara del Fuoco since 1868: reconstructing the effusive activity at Stromboli volcano. Bull. Volcanol. 74 (1), 231–248.

Massonnet, D., Feigl, K.L., 1998. Radar interferometry and its application to changes in the Earth's surface. Rev. Geophys. 36 (4), 441–500.

Mattox, T.N., Mangan, M.T., 1997. Littoral hydrovolcanic explosions: a case study of lava–seawater interaction at Kilauea Volcano. J. Volcanol. Geotherm. Res. 75 (1), 1–17.

Nemec, W., 1990. Deltas – remarks on terminology and classification. In: Coarse-Grained Deltas, pp. 1–12.

Nolesini, T., Di Traglia, F., Del Ventisette, C., Moretti, S., Casagli, N., 2013. Deformations and slope instability on Stromboli volcano: integration of GBInSAR data and analog modeling. Geomorphology 180, 242–254.

Poland, M.P., Orr, T.R., 2014. Identifying hazards associated with lava deltas. Bull. Volcanol. 76 (12), 880.

Poland, M.P., Peltier, A., Bonforte, A., Puglisi, G., 2017. The spectrum of persistent volcanic flank instability: a review and proposed framework based on Kīlauea, Piton de la Fournaise, and Etna. J. Volcanol. Geotherm. Res., 63–80.

Puysségur, B., Michel, R., Avouac, J.P., 2007. Tropospheric phase delay in interferometric synthetic aperture radar estimated from meteorological model and multispectral imagery. J. Geophys. Res., Solid Earth 112 (B5), 140–170.

Ramalho, R.S., Quartau, R., Trenhaile, A.S., Mitchell, N.C., Woodroffe, C.D., Ávila, S.P., 2013. Coastal evolution on volcanic oceanic islands: a complex interplay between volcanism, erosion, sedimentation, sea-level change and biogenic production. Earth-Sci. Rev. 127, 140–170.

Reid, M.E., Christian, S.B., Brien, D.L., 2000. Gravitational stability of three-dimensional stratovolcano edifices. J. Geophys. Res., Solid Earth 105 (B3), 6043–6056.

Reid, M.E., Christian, S.B., Brien, D.L., Henderson, S., 2015. Scoops3D – Software to Analyze Three-Dimensional Slope Stability Throughout a Digital Landscape. Tech. Rep. US Geological Survey Techniques and Methods, Book 14, p. 218.

Richards, A.F., 1959. Geology of the Islas Revillagigedo, Mexico, 1: birth and development of Volcan Barcena, Isla San Benedicto. Bull. Volcanol. 22 (1), 73–123.

Rotonda, T., Tommasi, P., Boldini, D., 2009. Geomechanical characterization of the volcaniclastic material involved in the 2002 landslides at Stromboli. J. Geotech. Geoenviron. Eng. 136 (2), 389–401.

Sansone, F.J., Smith, J.R., 2006. Rapid mass wasting following nearshore submarine volcanism on Kilauea volcano, Hawaii. J. Volcanol. Geotherm. Res. 151 (1), 133–139.

Stevens, N.F., Wadge, G., Williams, C.A., 2001. Post-emplacement lava subsidence and the accuracy of ERS InSAR digital elevation models of volcanoes. Int. J. Remote Sens. 22 (5), 819–828.

Tibaldi, A., Corazzato, C., Marani, M., Gamberi, F., 2009. Subaerial–submarine evidence of structures feeding magma to Stromboli Volcano, Italy, and relations with edifice flank failure and creep. Tectonophysics 469 (1), 112–136.

Tinti, S., Pagnoni, G., Zaniboni, F., 2006. The landslides and tsunamis of the 30th of December 2002 in Stromboli analysed through numerical simulations. Bull. Volcanol. 68 (5), 462–479.

Tommasi, P., Baldi, P., Chiocci, F.L., Coltelli, M., Marsella, M., Pompilio, M., Romagnoli, C., 2005. The landslide sequence induced by the 2002 eruption at Stromboli volcano. In: Landslides. Springer, Berlin, Heidelberg, pp. 251–258.

Voight, B., Elsworth, D., 1997. Failure of volcano slopes. Geotechnique 47 (1), 1–31.

Wadge, G., Webley, P.W., James, I.N., Bingley, R., Dodson, A., Waugh, S., Veneboer, T., Puglisi, G., Mattia, M., Baker, D., Edwards, S.C., Clarke, P.J., 2002. Atmospheric models, GPS and InSAR measurements of the tropospheric water vapour field over Mount Etna. Geophys. Res. Lett. 29 (19), 1–11.

Williams, S., Bock, Y., Fang, P., 1998. Integrated satellite interferometry: tropospheric noise, GPS estimates and implications for interferometric synthetic aperture radar products. J. Geophys. Res., Solid Earth 103 (B11), 27051–27067.

Zakšek, K., Hort, M., Lorenz, E., 2015. Satellite and ground-based thermal observation of the 2014 effusive eruption at Stromboli volcano. Remote Sens. 7 (12), 17190–17211.

Zebker, H.A., Rosen, P., Hensley, S., Mouginis-Mark, P.J., 1996. Analysis of active lava flows on Kilauea volcano, Hawaii, using SIR-C radar correlation measurements. Geology 24 (6), 495–498.